

Deep Learning Designs of Anisotropic Metasurfaces in Ultrawideband Based on Generative Adversarial Networks

Hai Peng Wang, Yun Bo Li,* He Li, Shu Yue Dong, Che Liu, Shi Jin,*
and Tie Jun Cui*

Metasurfaces have been developed as a promising approach for manipulating electromagnetic waves. Recently, deep learning algorithms have been introduced to design metasurfaces, but the network can only output one solution for each desired input and suffers from nonunique issue. To overcome the aforementioned challenges, a deep neural network model for inverse designs of anisotropic metasurfaces with full phase properties in ultrawideband is proposed. Given the target reflection spectra as inputs, the candidate metasurface patterns are generated through a generative adversarial network (GAN), and the corresponding predictions are simply achieved by the accurate forward neural network model to match the target spectra in the whole band with high fidelity. By training the generator and discriminator in GAN in an alternating order combined with setting a threshold of discriminator loss to trigger the phase prediction, the proposed method is much more efficient and consumes less time in the training process. Numerical simulations and experimental results demonstrate that the reflection phases of the generated meta-atoms have excellent agreements with the given targets, providing an efficient way in automatically designing metasurfaces. The most important advantage of this approach over the previous schemes is to improve the design speed significantly with very good accuracy.

advantages of low loss, easy fabrication, low profile, and unique EM properties, many metasurfaces have been designed for versatile applications, such as vortex beam generators,^[4] polarization converters,^[5,6] perfect absorbers,^[7,8] and amplitude and phase modulators.^[9] More recently, digital coding and programmable metasurfaces have been introduced.^[10] Using the active devices to control the digital states of meta-atoms electrically, the programmable metasurfaces have led to numerous novel devices and systems, including programmable holograms,^[11] microwave imaging,^[12,13] and new-architecture wireless communication systems.^[14–17]

Traditionally, for a set of given target parameters, the general methods for designing the metasurfaces are mainly based on trial and error with iterative optimizations,^[18,19] in which the iterative optimization approaches can be classified into two types: adjoint-based topology^[20,21] and genetic algorithm optimization.^[22,23]

Although such design methods can produce acceptable results, it remains a big challenge to deploy them in large and realistic scenes due to the large numbers of meta-atom structures, high computational costs, and time-consuming numerical simulations. To resolve such difficulties, deep learning methods have attracted the increasing attention recently in designing the metasurfaces. During the past 2 years, the deep learning has shown as a fastest-growing machine learning method for addressing complex and processing tasks due to the increasing amount of big data and ever-increasing computational power.^[24,25] The deep learning approaches such as deep neural networks (DNNs) can learn the complicated data characteristics and relationships between inputs and outputs, and then use multilayered neural networks to automatically set up nonlinear models for abstractive representations. Some scientists have designed various fully optical or acoustic machine learning hardware platforms with physical inhomogeneous medium to perform fast and efficient DNN analog computation,^[26–29] and achieved comparable object recognition^[26,27] and vowel classification^[28,29] performance to the standard digital DNN implementations.


In addition, DNNs have shown efficient “forward-design” that can approximate the physical spectrum response to replace with numerical simulation in orders of magnitude less time,

1. Introduction

As 2D subwavelength structures with different geometries and distributed functional arrangements, metasurfaces^[1–3] have been developed as a promising means for dynamically and arbitrarily manipulating electromagnetic (EM) waves. Due to the

Dr. H. P. Wang, Prof. Y. B. Li, H. Li, S. Y. Dong, C. Liu, Prof. T. J. Cui
State Key Laboratory of Millimeter Waves
Southeast University
Nanjing 210096, China
E-mail: moztaiyunbo@163.com; tjcu@seu.edu.cn

Dr. H. P. Wang, Prof. S. Jin
National Mobile Communications Research Laboratory
Southeast University
Nanjing 210096, China
E-mail: jinshi@seu.edu.cn

 The ORCID identification number(s) for the author(s) of this article can be found under <https://doi.org/10.1002/aisy.202000068>.

© 2020 The Authors. Published by WILEY-VCH Verlag GmbH & Co. KGaA, Weinheim. This is an open access article under the terms of the Creative Commons Attribution License, which permits use, distribution and reproduction in any medium, provided the original work is properly cited.

DOI: 10.1002/aisy.202000068

and perform the inverse design of microwave and optical device structures.^[19,30–34] The general procedures are mainly setting up DNNs to construct matchings between the structures and EM properties by implementing sufficient EM simulations with variable structure parameters and corresponding spectrum response at selected frequency bands or wavelength. Then, the trained network can be adopted to solve inverse design metasurfaces,^[19,30] wavelength demultiplexer,^[31] and power splitters^[32] using back propagation, where the input takes the EM design targets such as light scattering, transmission, and reflection spectra. This inverse network has one-time structural parameter output, with the advantage of automatic process, fast speed, and less computational resource-consuming. However, it encounters the following problems. First, the network can only output one solution for each desired input and cannot find the optimal solutions. Second, it suffers from nonuniqueness issue, which makes it difficult to train neural networks on a tremendous training data set. An iterative process using binary particle swarm optimization (BPSO) has been proposed to optimize the metal patterns of the meta-atom structures to fulfill the desirable anisotropic phase inverse design.^[33] In contrast, Liu et al. proposed to use a tandem architecture,^[34] which is composed of an inverse design network connected to a forward modeling network, and can directly output the device structures without iterative optimization process. It can allow DNNs to be effectively trained with datasets containing nonunique EM scattering issue. However, when using coding patterns that contain centrosymmetric square metal subblocks, the training difficulty of free-form geometry meta-atoms will further limit its anisotropic applications, due to the randomness and diversity of the discrete coding lattices.

Recently, the concept and method of inversely designing anisotropic metasurfaces based on generative adversarial network (GAN) was proposed.^[35] Subsequently, conditional deep convolutional GAN was also introduced to design nanophotonic structures and metagratings.^[18,36] Combined with the concepts of conditional GAN^[37] and Wasserstein GAN (WGAN),^[38] the generative model was incorporated into a simulator (another DNN) to jointly calculate the meta-atom patterns for intended transmission spectra.^[35] The GAN model can overcome the challenge of nonuniqueness in inverse design, and the guided shape geometry can avoid training convergence difficulty due to the data diversity and randomness. However, compared with these references which mainly demonstrated the inverse design metasurface and optical devices with amplitude responses, the phase response prediction and inverse design has not to be studied. The main challenge in the phase design is because of the phase discontinuities at π -phase, which is caused by the equivalent electric and magnetic dipoles with resonances existing in the metadevices.^[39] The only anisotropic phase prediction using machine learning has demonstrated an accuracy of 90.05% of phase responses with 2° error in the 360° phase.^[33] However, it can only predict the phase at a single frequency point with trained neural network, and will be time-consuming to design wideband anisotropic metasurfaces. Therefore, the phase discontinuities and wideband design have become the limitation of designing phase-sensitive reflectarrays, metalenses, and stealth surfaces using deep learning. In addition, the average training time for 10 000 iterations for a desirable target mentioned in the study by Liu et al.^[35]

is about 10 min. Therefore, the training process needs to be optimized to reduce the design cost.

In this work, we propose to design the anisotropic metasurfaces with full phase properties in ultrawideband based on the GAN network. Given the required or target reflection spectra as input, the candidate metasurface patterns with irregular shapes are generated by setting up a conditional deep convolutional GAN (cDCGAN). We train the generator and discriminator in the network using an alternating order with different loss functions from those in the study by Liu et al.^[35] and trigger the phase prediction through setting a threshold of discriminator loss. We can reduce the number of generated patterns for phase predictions and target-distance calculations. Thus, the proposed GAN-based network is much more efficient and consumes much less time in the training process. The corresponding phase predictions can be simply achieved by an accurate forward neural network model, which is incorporated with the GAN model constituting a loop to successively match the target spectra in the whole band with high fidelity. According to the numerical simulations and experimental measurements, the generated reflection phases in the ultrawideband of transverse-electric (TE) and transverse-magnetic (TM) polarized waves have excellent agreements with the given targets, providing efficient and fast method in automatic designs of the metasurface structures to achieve the required anisotropic reflective phase responses in ultrawide frequency band.

2. Experimental Section

2.1. Inverse Designs of Metasurface Based on GANs

The traditional metasurface design process mainly includes the specialized EM knowledge requirements, meta-atom structure modeling, and iterative forward numerical EM simulations with parameter sweeping and optimization, which need high computational resources and time costs. The neural networks had previously been used to approximate the physical responses, which we called “forward prediction.” Once the forward neural network models are trained, the inversely approximate designs for a targeted optical response can be addressed, which we called “inverse design.” Herein, we proposed a new GAN-based inverse design method to realize fast, efficient, and automatic designs of metasurfaces with anisotropic reflection responses. The overview of the new design process is shown in **Figure 1**. On the one hand, similar to the previous schemes, it contains a forward DNN predictor trained from a constructed dataset composed of various geometric data (binarized meta-atom pattern images) and the corresponding reflective spectra, which can predict the amplitude and phase responses of a meta-atom structure in a few seconds with very high accuracy. On the other hand, a GAN network was trained with the geometric data for the purpose of inverse designs. When the input reflective spectra are given, the candidate patterns can be generated through the GAN-based network. The corresponding phase and amplitude predictions were directly achieved from the accurate forward DNN predictor, and matched with the target spectra in high fidelity by the Euclidean distance calculation. Finally, the matched pattern

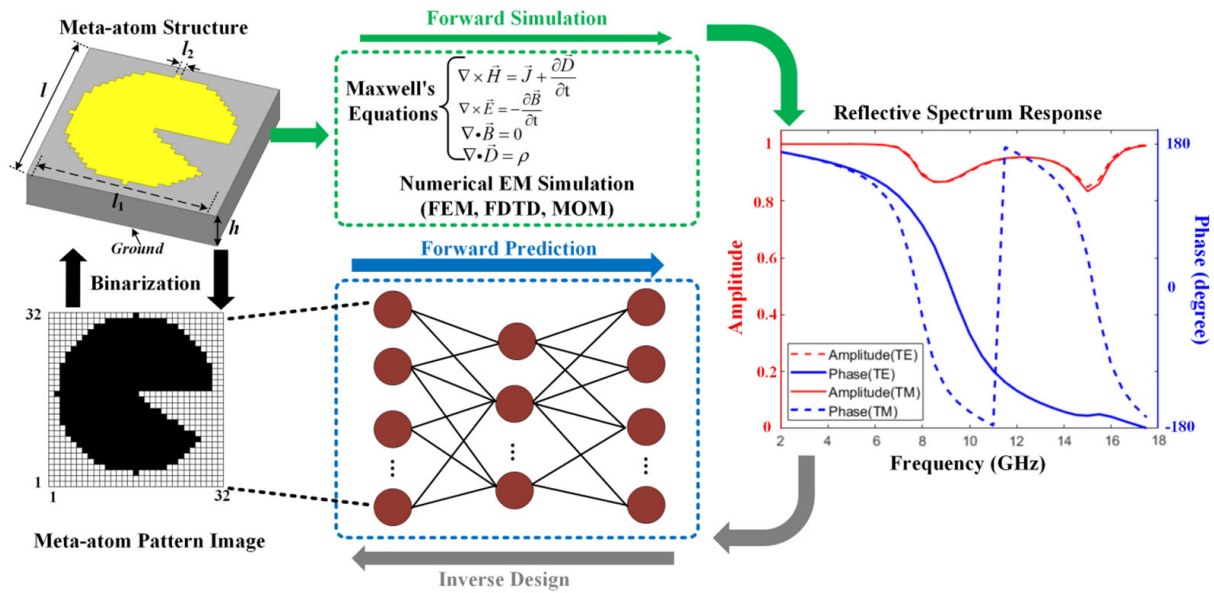


Figure 1. The overview design process of metasurfaces for anisotropic reflective spectra, which includes the conventional numerical EM simulations, forward prediction, and inverse design process based on the neural network.

represented as pixelwise image was selected and fabricated as the metal layer of the meta-atom.

2.2. Structures of Meta-Atoms

A general single-layer structure of the meta-atom used in this design is shown in Figure 1. The meta-atom is composed of 32×32 binary pixel image as the description of 32×32 lattices, in which pixel “0” (black) means the part covered with metal and pixel “1” (white) means without metal. This introduced the concept of image and integrated the deep learning algorithms to the design procedure. The size of each lattice was set to $l_2 = 0.3$ mm, and the lengths of the unit cell and metal pattern were depicted as the parameters $l = 10$ mm and $l_1 = 9.6$ mm, respectively. The thickness of metal layer was 0.018 mm. A commercial F4B dielectric spacer was used as the dielectric substrate with

thickness $h = 2$ mm, dielectric constant $\epsilon_r = 2.65$, and loss tangent $\tan \delta = 0.003$. The other side of the F4B substrate was covered by copper and used as ground plane.

2.3. Neural Network Architecture

Figure 2 shows the neural network architecture of the proposed GAN-based inverse design method, which mainly consists of three deep convolutional networks, a generator (G), a discriminator (D), and a predictor (P). The generator and discriminator constitute a conditional DCGAN (cDCGAN), which takes the target reflection-phase data and 32×1 size random noise vector as the input. The reflection-phase data included 32×1 size for TE and 32×1 size for TM polarized waves, respectively. The total 96×1 size input data formed random points in the latent space, and the generator can decode them into a composite image with 32×32 pixels.

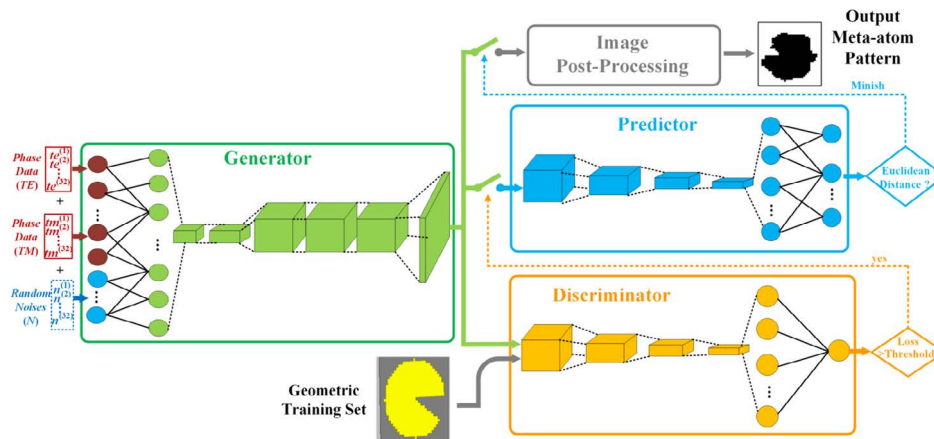


Figure 2. Architecture of the proposed GANs-based inverse design method.

Then, the composite image and the predefined geometric training set were simultaneously sent to the discriminator. The discriminator can help to predict whether the pattern was from the training set or created by the generator. The generator was trained to enable it to deceive the discriminator, and could gradually generate more and more realistic images, which seemed to be indistinguishable from real images, so that the discriminator could not distinguish between the two sets. Different from the previous GAN schemes, here we set a threshold for the discriminator loss based on fact that DCGAN can provide a stable Nash equilibrium solution,^[35] so that we can select more suitable samples to send into the predictor model. The predictor is a pre-trained neural network, which takes the generated 32×32 pixel image as input and predicts its reflection coefficients of TE and TM waves in a few seconds with high accuracy. Then, the Euclidean distance between the predicted reflection spectra and targeted spectra was calculated. Once the distance is decreased, the corresponding generated image will be postprocessed and saved. After the iterative training and generation of the network finish, the pattern corresponding to the minimum distance was selected as the final output of the metal pattern for the meta-atom. The detailed structures and configurations of the proposed neural network model are shown in the Supporting Information S1.

2.4. Training Process

According to the GAN theory^[40] and previous study,^[35] the geometric data from predefined geometric training set were defined as s , and the composite images produced by the generator were s' . Their corresponding simulated reflection coefficients were denoted as R and R' , respectively. The generator G and the discriminator D were working in the adversarial mode which was similar to the two-player minimax game with the following value function

$$\min_G \max_D V(D, G) = E_{s \sim p_{\text{data}}(s)} [\log D(s)] + E_{(R, z) \sim p_{(R, z)}(R, z)} [1 - \log D(G(R, z))] \quad (1)$$

where the geometric data of training set input to the discriminator is denoted as s , and the noise input to the generator is denoted as z . Thus, (R, z) was combined as the condition data input to the generator of cDCGAN. In addition, the term $D(x)$ represents the probability that the input pattern x comes from the geometric training set s , and $D(G(R, z))$ represents that the generated design $G(R, z)$ is recognized as from s . According to this value function, the weights of G and D should be trained and updated simultaneously to maximize the accuracy probability in discriminating both the training dataset and samples from G , while training G to minimize $\log(1 - D(G(R, z)))$.

In practice, the aforementioned equation has difficulty for providing sufficient gradients for the generator to learn well and cause $\log(1 - D(G(R, z)))$ saturating easily.^[34] In our work, we presented a training method to train G and D in an alternating order. During the training process, it included discriminator training and generator training. Note that the discriminator needs to be set to frozen (not trainable) so that its weight will not be updated when training the generator. The detailed training process and algorithm derivation are given in Supporting

Information S2. Based on the derivation, the loss functions of discriminator and generator can be calculated as

$$L_D = -\frac{1}{m} \sum_{i=1}^m [\log(D(G(R, z^{(i)})))] - \frac{1}{m} \sum_{i=1}^m [\log(1 - D(s^{(i)}))] \quad (2)$$

$$L_G = -\frac{1}{m} \sum_{i=1}^m [\log(1 - D(G(R, z^{(i)})))] \quad (3)$$

where m is the batch size, and the superscript i indicates the i th data in the batch.

In training the predictor P , because it is a model for solving a scalar regression problem, which predicts a continuous spectrum value rather than a discrete label, the last layer of the network is a linear layer without activation, and the model P can learn to predict the values in an arbitrary range. The mean squared error (MSE) was used as the loss function of the predictor, which was defined as the square of difference between the predicted value (R') and the simulated value (R).

After the training predictor was finished, we began the GAN training. In each GAN training iteration, the weights of the generator and the discriminator were updated in an alternating order. Because L_D defines the resemblance between the geometrical data and generated patterns, and L_G defines the mismatch between the two classes, the candidate patterns can be generated in the training process when meeting the condition that L_D achieves the maximized value, whereas L_G is minimized. Next, we set a threshold for the discriminator loss L_D . When L_D exceeds this threshold for each iteration, the generated pattern by the generator will be fed into the predictor P to achieve the anisotropic reflective spectrum data R'' . Then, compute the Euclidean distance l_{dist} between the predicted phase data R'' and the target phase data R

$$l_{\text{dist}} = \sqrt{\sum_{j=1}^n (R_j - R''_j)^2} \quad (4)$$

where n is the total size of the reflection coefficient phase data points, and the superscript j indicates the j th data point of normalized R'' and R . When the condition of l_{dist} diminished occurs, the correspondingly generated pattern is saved during the GAN training iteration, until the end of the training process. Finally, the last updated minimized l_{dist} and the generated pattern will be selected and postprocessed to binary images as the candidate patterns of the meta-atom for the targeted anisotropic reflective phase performance.

2.5. Training Datasets

We collected a dataset containing nearly 5000 different geometric shapes with five classes (circle, arc, sector, ring, and modified Mixed National Institute of Standards and Technology (MNIST) handwritten digital dataset). Then, using these geometric shapes to replace the metal layers of the meta-atom structures, the corresponding anisotropic reflective spectrum data were simulated using the commercial EM software ANSYS HFSS 2018. Finally, by adding random noise into the pixel images, shifting and rotating meta-atom patterns, we constituted a total number

of 10 000 samples for the predictor training set, where the meta-atom structure represented by a 32×32 binary pixel image was the input data, and the corresponding anisotropic reflective spectrum data were the output data. The detailed information of the geometric training datasets is presented in Supporting Information S3.

3. Results and Analysis

According to the description of the neural network architecture and design process, we can learn that the generator and discriminator with cDCGAN are responsible for generating various patterns, whereas the predictor is in charge of filtering appropriate candidate through estimating the reflection phase and calculating the distance with the target object. Therefore, the accuracy of the predictor is crucial for the entire inverse design. In this section, we first validate the pretrained predictor to make sure that it works with high fidelity. Then, combining the predictor with cDCGAN, we conduct two tests for the demonstration of the whole network, which can realize automatic inverse designs of metasurfaces under the on-demand set of reflection phases. We remark that all deep learning models (G , D , and P) are performed on a workstation with an Intel Xeon E5-4210v2 @2.2 GHz central processing unit, NVIDIA GeForce GTX 2080Ti, and 128 GB access memory; and the deep learning frameworks Tensor Flow and Keras are used to design and train the networks.

3.1. Predictor Performance

We randomly select 75% of the predictor training set as the training part, and the other 25% of the dataset as the validation part to test its prediction accuracy. The MSE that is defined as the square of difference between the predicted value (\hat{R}_i) and the target value (R_i) is used as the loss function of the predictor. The mean absolute error (MAE) is used as the evaluation metric of predictor training and testing, which is the absolute value of the difference between the predicted and target values.

The detailed network training hyperparameters are shown in Supporting Information S2. **Figure 3a** shows the variation of the loss and evaluation metric during training the predictor. The average training loss and training MAE are converged, respectively, to less than 0.001 and 0.01 after 10 000 steps. According to validation test, the pretrained predictor can estimate the reflection coefficient R with an average absolute error of less than 0.02 for each pattern in the geometric dataset. **Figure 3b** shows the prediction performance of the predictor with a geometric sample from the validation set. The solid lines are simulated spectra R of metasurfaces with the sector pattern as the metal layer in the element presented in the inset of **Figure 3b**. They are, respectively, the amplitudes (pink) and phases (red) of the reflection coefficients with the TE mode, and amplitudes (black) and phases (blue) with the TM mode. For comparison, the red and blue circles are respectively shown in **Figure 3b**, representing the reflective phase performance $\hat{R}_{\text{phase_TE}}(f)$ and $\hat{R}_{\text{phase_TM}}(f)$ approximated by the trained predictor. However, the pink and black crosses are the predicted reflective amplitudes $\hat{R}_{\text{amplitude_TE}}(f)$ and $\hat{R}_{\text{amplitude_TM}}(f)$. Each group of reflective amplitude and phase response data is expressed as a vector of 32-dimension with equal frequency spacing in the ultrabroadband from 2 to 18 GHz. We see that the circles and crosses nearly have coincidence in each group, showing good agreements with the simulated results. Some additional samples selected from different geometric classes compared with the simulated results are presented in Supporting Information S4.

3.2. Inverse Design Test under the Target Phase of Geometric Dataset

The proposed GANs-based network is evaluated on specified test samples from different geometric datasets as the input target phases, making the framework search appropriate patterns for these spectral targets. At the input of the generator, we randomly select a set of reflection phase spectra $R_{\text{phase_TE}}(f)$ and $R_{\text{phase_TM}}(f)$ from 2 to 18 GHz, with the number of 200 samples from each geometric class with the anisotropic properties (including sector, arc, and modified MNIST handwritten digital

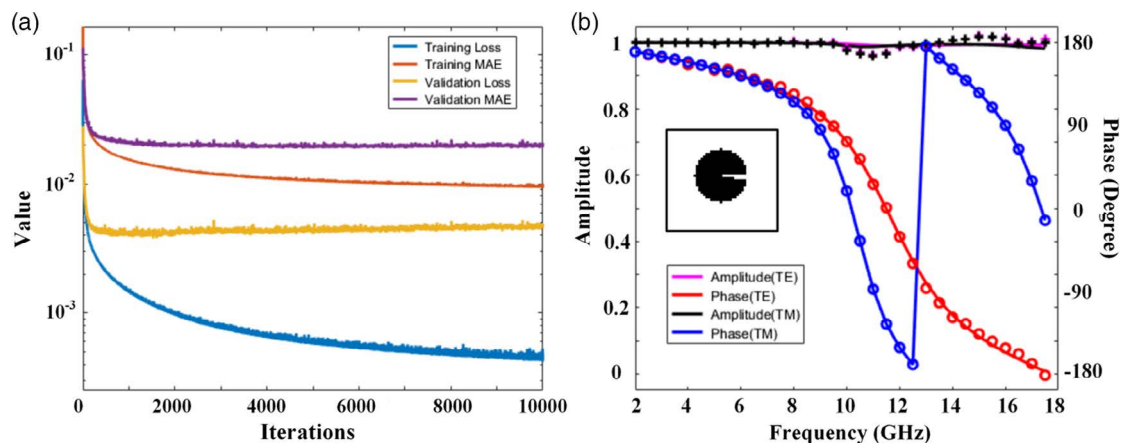


Figure 3. Effectiveness of the pretrained simulator. a) The variation of the loss and evaluation metric during the training of predictor, from which the average training loss and training MAE are, respectively, converged to less than 0.001 and 0.01 after 10 000 steps. b) The prediction performance of the predictor with one geometric test sample (the inset) from the validation set.

dataset). The detailed network (G and D) training hyperparameters are available in Supporting Information S2. The batch size is set to 16, which means the number of patterns to seek out in each training iteration. For each group of input target reflection phases, the geometrical training set fed into discriminator is composed of 1000 randomly chosen values from the same geometric class. In addition, the threshold for generating the candidate patterns is optimized to 0.4, which can significantly save the training time, because it can narrow down the number of generated patterns for phase predictions and target-distance calculations. It takes about 3.5 min in average to perform the total 10 000 iterations of training on the workstation with a GPU GTX 2080Ti for one targeted inverse design.

Figure 4 shows the inverse design results of generated patterns under the target phases. The anisotropic reflection phase data of the sector test sample (Figure 4a) and the modified MNIST handwritten digital test sample (Figure 4b) are respectively

fed into the network. The solid curves are the simulated anisotropic phases of the test samples s (the upper right inset), whereas the circles are the simulated responses of the generated patterns s' (the lower right inset). The comparison results show excellent agreements between the generated patterns and the test samples. Some additional samples are presented in Supporting Information S5.

At the same time, the quantitative evaluation is conducted. Two metrics are introduced to quantify the generated performance: 1) MAE is defined as the average difference between the target anisotropic reflection phases of per frequency point (R_i) and the responses (R'_i) of the generated element; 2) average accuracy represents the average similarity between the two normalized reflection phase data, which are defined as

$$\text{Accuracy}_{\text{avg}} = 1 - \frac{1}{360n} \sum_{i=1}^n |R_i - R'_i| \quad (5)$$

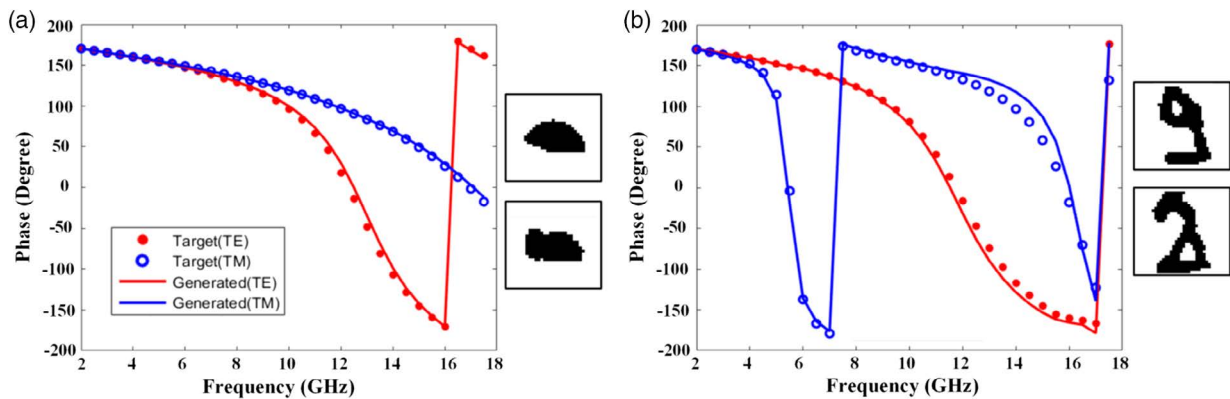


Figure 4. The anisotropic reflection phase responses of generated patterns with a predesigned class of geometric data. a) The sector test sample. b) The modified MNIST handwritten digit test sample. In each figure, the solid curves are the simulated anisotropic phases of the test samples s (the upper right inset), whereas the circles are the simulated responses of the generated patterns s' (the lower right inset).

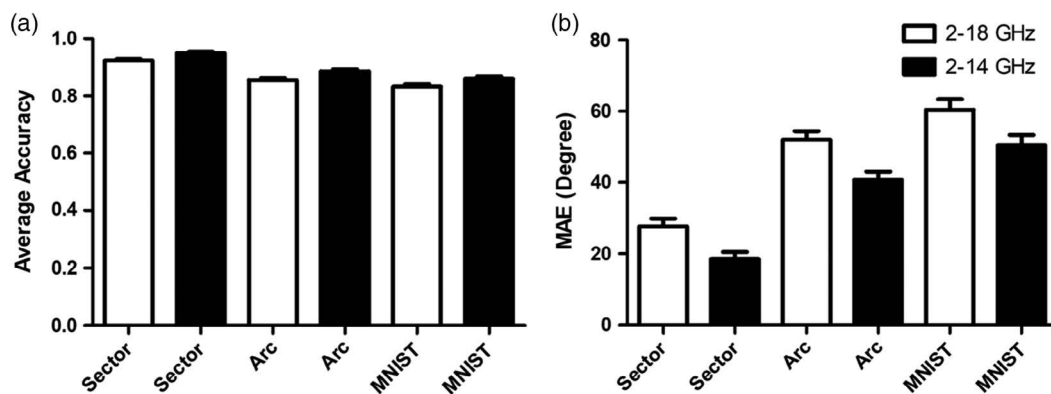


Figure 5. Statistical metrics of the inverse design test under the target phase of three geometric classes with anisotropic property. a) Average accuracy within three classes of geometric data. b) MAE within three classes. Consistent with ref. [35], these statistical metrics are counted based on the test samples whose generated patterns are in the same geometric class. The geometric accuracies of these tests are 0.89 (sector), 0.79 (arc), and 0.74 (MNIST). The white boxes in the figure mean that the results are calculated in the frequency range from 2 to 18 GHz, whereas the black ones are in the frequency range from 2 to 14 GHz. The mean average accuracies of the generated phase performance in the range 2–18 GHz are 0.92 (for the sector), 0.86 (for the arc), and 0.83 (for the MNIST). The accuracies can be respectively improved to 0.95, 0.89, and 0.86 in the range 2–14 GHz. Similarly, MAEs are $27.7^\circ \pm 2.1^\circ$, $52.0^\circ \pm 2.4^\circ$, and $60.4^\circ \pm 3.0^\circ$ within 2–18 GHz, and $18.6^\circ \pm 1.9^\circ$, $40.8^\circ \pm 2.2^\circ$, and $50.4^\circ \pm 3.0^\circ$ within 2–14 GHz.

Consistent with ref. [35], the aforementioned statistical metrics are counted based on the test samples whose generated patterns are in the same geometric class. **Figure 5** shows the means and standard error means (SEMs) of the statistical metrics for three geometric classes. We can learn that the proposed method have better performance in the ultrawide frequency range from 2 to 14 GHz.

3.3. Inverse Design Test under the User-Defined Target Phase

Finally, the proposed GANs-based network is tested for inverse design of a metasurface with user-defined phase responses. The meta-atom of metasurface can be represented by a simple lumped equivalent circuit model, as shown in the inset of **Figure 6a**. Therefore, we define four types of ideal anisotropic phase curves by setting different values of inductor and capacitor. Using the combination of phase-curve slope (fast and slow), we called them “FF,” “SS,” “FS,” and “FS” types, respectively. The detailed description of the meta-atom equivalent circuit model and parameters for the four types of ideal anisotropic phase curves are presented in Supporting Information S6.

For each type of ideal anisotropic phase curve, multiple patterns can be generated from proposed GANs-based network.

There are mainly three means to obtain multiple patterns. 1) Repeat the iterative training and generation of the network using same input. Because of the randomness and diversity of the generator in the GAN, candidate patterns with different shapes can be generated. 2) Using different geometric data can make the discriminator guide the generator to achieve more candidate patterns in the inverse design process. 3) Extract different target information (such as different frequency band) from the target phase curve and send it as the input of the network.

The “FF” type of ideal anisotropic phase curves and lumped equivalent circuit model (inset) are shown in the inset of **Figure 6a**. The “FF” type target curves are solved by method 1 (repeating method), and two shapes (samples a and b) are selected as the final patterns under the guide of sector geometric dataset. **Figure 6b,c** shows the two patterns (inset) generated by repeated iterative training and generation. The corresponding reflection phases for these two solutions are simulated in the ANSYS HFSS 2018 for the verification. The two anisotropic reflection phase curves of the generated patterns (samples a and b) all agree well to the target ones. The average accuracy is 0.92 and MAE is 28.48° for sample a, and the average accuracy is 0.90 and MAE is 36.37° for sample b. For the frequency range of 2–14 GHz, the performances are better, where the average accuracy are 0.98 and 0.98, and MAE are 6.5° and 5.5°, respectively.

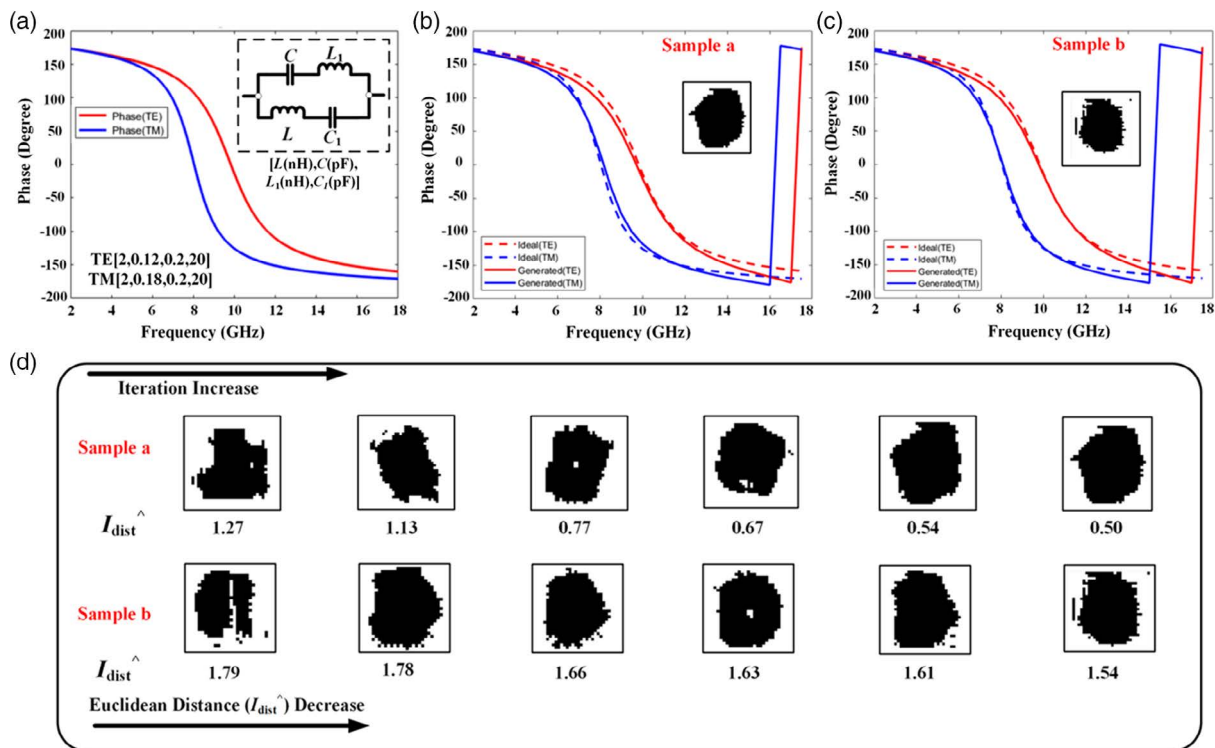


Figure 6. The generated patterns for the user-defined target anisotropic reflective phases. a) The user-defined “FF”-type anisotropic reflective phase curves designed by a simple lumped equivalent circuit model (the inset) to represent the meta-atom. The detailed model parameters for the user-defined phase curves of TE and TM polarized waves are defined in the form of a vector $[L_1(\text{nH}), C_1(\text{pF}), L_2(\text{nH}), C_2(\text{pF})]$. b,c) The generated meta-atom patterns (the insets) and the correspondingly simulated reflection phases for solving the “FF”-type case. The two reflection phase curves of the generated patterns agree very well to the target ones. d) The generated images selected from the iterative inverse design process of “FF”-type case when the condition of Euclidean distance I_{dist} diminished occurs. The images in the top row are corresponding to sample a, and the bottom row are for sample b. The last updated minimized I_{dist} and the generated pattern will be selected and postprocessed to binary images as the candidate patterns of the meta-atom for the targeted anisotropic reflective phase performance.

We also tested the proposed GANs-based neural network on the other three types of target phases with the aforementioned methods to get multiple alternative solutions. The detailed results are shown in Figure S8 and Table S2, Supporting Information S6. The “SS” and “FS” type target curves are using method 2 (using different geometric data). The predefined geometric classes for the “SS” type are sector (sample c) and modified MNIST handwritten digital dataset (sample d), whereas the sector and arc datasets are selected for the inverse design of “FS” type, and the solutions are corresponding to samples e and f. Finally, the “SF” type of case is realized by method 3, and two different frequency bands 2–14 GHz and 2–18 GHz are extracted and sent as the input, respectively. The multiple solutions are samples g and h. From the results in the Supporting Information, we can obtain the mean average accuracy of 0.89 with MAE 41.56°. Especially for the frequency range of 2–14 GHz, the mean average accuracy is 0.96 with MAE of 13.97°.

To display the design process of the network, Figure 6c shows the generated patterns selected from the iterative inverse design process of “FF” type case when the condition of Euclidean distance \hat{l}_{dist} diminished occurs. The patterns in the top row are corresponding to the process of obtaining sample a, and the ones in the bottom row are for the sample b. It can be seen that, with the solving iteration of network increases, the \hat{l}_{dist} of pattern from left to right decreases in turn. Finally, the last updated minimized \hat{l}_{dist} and the generated pattern will be selected and postprocessed to binary images as the candidate patterns of the meta-atom for the targeted anisotropic reflective phase performance. In addition, Figure S9 and S10, Supporting Information S6, show the generated patterns selected in the iterative process for inverse design of four types of ideal anisotropic phase curves and the corresponding EM simulations of reflection phases. The detailed evaluation metrics of these generated patterns (the insets in Figure S9 and S10, Supporting Information) are shown in Table S3 and S4, Supporting Information S6.

To verify our proposed concept and design, a prototype of anisotropic metasurface using the meta-atom pattern shown in Figure 6b was fabricated and measured. The manufactured

sample had the size of $250 \times 250 \text{ mm}^2$, and the experimental setup for near-field measurements in the microwave quasioptical test platform is shown in Figure 7a. The sample was placed in the center of the platform, and the lens which can generate the quasipplane wave was connected with Agilent N5230C PNA-L Microwave Network Analyzer. The measured results are shown in Figure 7b, in which the measured frequency spans from 4 to 18 GHz. It is evident that the proposed metasurface can achieve good agreements in the range of 4–14 GHz, with the average accuracy of 0.92 and MAE of 30.5°.

4. Discussion

As far as we know, there is no reference investigating whether minor modification of the lattice distribution has a macroscopic influence to the numerical reflective response. Only Liu et al.^[35] described that three augmented operations (including adding random noise into the pixel images, shifting and rotating meta-atom patterns with 180°) will not modify the numerical reflective response. However, if only change few pixels to the opposite value in the lattices, the influence to the simulated reflective spectrum has yet to be studied.

First, from these generated patterns shown in Figure S9 and S10, Supporting Information S6, we can find that the proposed generator of GAN network can generate similar images with minor modification of the lattice distribution, such as sample groups (a5, a6), (c5, c6), (d5, d6), (e5, e6), (f2, f3), (h1, h2), and (h4, h5, h6). At the same time, Table S3 and S4, Supporting Information S6, show the corresponding \hat{l}_{dist} and I_{dist} evaluation metrics, which are the Euclidean distance based on the predicted phase data and simulated phase data, respectively. Most of these two metrics have the same changing trend, except for individual samples (e.g., samples f3 and g5). Therefore, we can conclude that our proposed GAN-based network is sensitive to the minor change in the pattern distribution, which means it can generate minor change and distinguish the corresponding influence.

Second, from the simulated reflective response of sample groups (a5, a6), (c5, c6), (e5, e6), (h1, h2), and (h4, h5, h6),

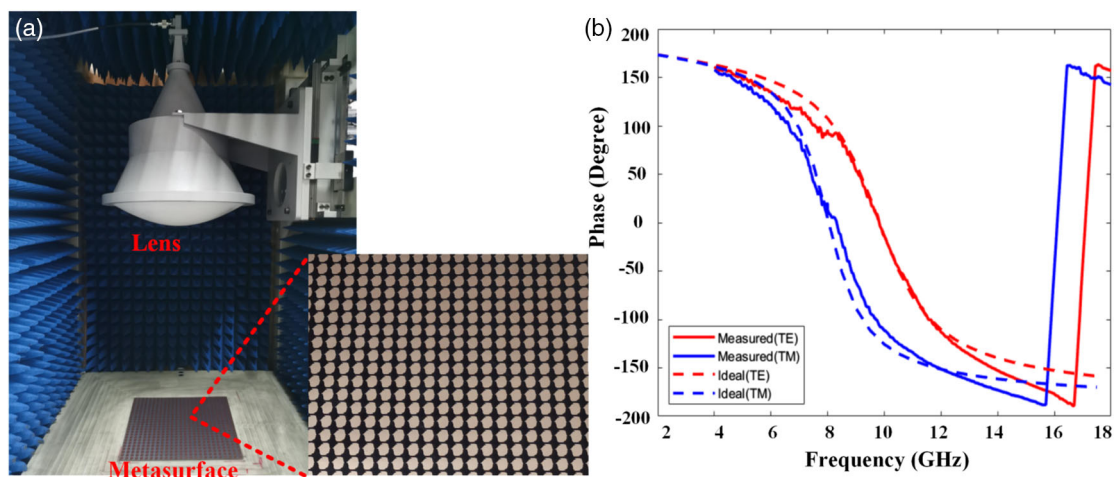


Figure 7. a) Experimental setup for the near-field measurements in the microwave quasioptical test platform. b) The measured results of the manufactured sample using the generated meta-atom pattern shown in Figure 6b.

we can find that all these sample groups have nearly same numerical reflective response, except the sample groups (d5, d6) and (f2, f3). These two groups have significantly different results. We consider that this minor modification in the patch may cause the phase discontinuities due to the resonances in the meta-atom structure. Therefore, the minor modification of the lattice distribution in the patch may not have a macroscopic influence to the numerical reflective response under normal cases, except the condition of generating the resonances within the metadevices. Further researches are needed to conduct this question.

In addition, the automatic design of metasurfaces for the user-defined phase responses demonstrates significant difference between the generated meta-atom patterns and feeding guided geometries. It means that the generated meta-atom patterns are completely irregular and beyond the constraints of the predefined shapes. Therefore, we can infer that the accurate predictor, filtering the suggested candidates by estimating and calculating the distance with the target phases, plays an import role in the whole inverse design.

Nevertheless, there are still two aspects to be considered to improve this research: 1) The larger dataset with more shape classes will result in higher fidelity. Therefore, the dataset needs more geometric classes, such as square, rectangular, triangular, cross, L-shape, V-shape, H-shape, and even the metagratings produced by the generator,^[18,35] so that we can supply a much more comprehensive dataset. It will help to further improve the accuracy of the predictor when the network is facing with various patterns. At the same time, the discriminator can guide the generator to achieve more candidate patterns which are much closer to the target. 2) More meta-atom structural parameters need to be considered in the neural network, such as the substrate thickness, dielectric constant, size, and multiple layers in the meta-atoms of metasurface, which can overcome the existing physical and structural prediction limits.

5. Conclusion

We proposed the GAN-based neural network to inversely design anisotropic metasurfaces with full phase properties in ultrawideband. Based on the numerical simulations and experimental measurements, the proposed method can realize the mean average accuracy as high as 0.96 for the four types of user-defined target reflection phases in the ultrawideband frequency range of 2–14 GHz, with the MAE of 13.97°. It takes about 3.5 min in average to perform the inverse design of metasurfaces for one on-demand input target. Compared with the conventional design methods, it can significantly improve the design speed with good accuracy. Accordingly, many applications such as designing the reflect-arrays, metalenses, and stealth surfaces will be benefit from the proposed method.

Supporting Information

Supporting Information is available from the Wiley Online Library or from the author.

Acknowledgements

This work was supported by the National Key Research and Development Program of China (grant nos. 2017YFA0700201, 2017YFA0700202, and 2017YFA0700203), the National Natural Science Foundation of China (grant nos. 61801262, 61901113, 61631007, and 61571117), the Natural Science Foundation of the Jiangsu Higher Education Institutions of China (grant no. 18KJB510039), and SEU-NJMU Joint Fund (grant no. 3204009351).

Conflict of Interest

The authors declare no conflict of interest.

Keywords

anisotropic reflective phase response, generative adversarial networks, inverse designs, metasurfaces, ultrawideband

Received: April 6, 2020

Revised: May 6, 2020

Published online:

- [1] C. L. Holloway, E. F. Kuester, J. A. Gordon, J. O. Hara, J. Booth, D. R. Smith, *IEEE Antennas Propag. Mag.* **2012**, *54*, 10.
- [2] A. V. Kildishev, A. Boltasseva, V. M. Shalae, *Science* **2013**, *339*, 1232009.
- [3] X. B. Yin, Z. L. Ye, J. Rho, Y. Wang, X. Zhang, *Science* **2013**, *339*, 1405.
- [4] M. Q. Mehmood, S. Mei, S. Hussain, K. Huang, S. Y. Siew, L. Zhang, T. Zhang, X. Ling, H. Liu, J. Teng, A. Danner, S. Zhang, C. W. Qiu, *Adv. Mater.* **2016**, *28*, 2533.
- [5] P. C. Wu, W. Zhu, Z. S. Shen, P. H. J. Chong, W. Ser, D. P. Tsai, A. Q. Liu, *Adv. Opt. Mater.* **2017**, *5*, 1600938.
- [6] B. Q. Lin, J. X. Guo, P. Chu, W. J. Huo, B. G. Huang, L. Wu, *Phys. Rev. Appl.* **2018**, *9*, 024038.
- [7] S. Savo, D. Shrekenhamer, W. J. Padilla, *Adv. Opt. Mater.* **2014**, *2*, 275.
- [8] G. M. Akselrod, J. Huang, T. B. Hoang, P. T. Bowen, L. Su, D. R. Smith, M. H. Mikkelsen, *Adv. Mater.* **2015**, *27*, 8028.
- [9] L. Liu, X. Zhang, M. Kenney, X. Su, N. Xu, C. Ouyang, Y. Shi, J. Han, W. Zhang, S. Zhang, *Adv. Mater.* **2014**, *26*, 5031.
- [10] T. J. Cui, M. Q. Qi, X. Wan, J. Zhao, Q. Cheng, *Light: Sci. Appl.* **2014**, *3*, e218.
- [11] L. Li, H. X. Ruan, C. Liu, Y. Li, Y. Shuang, A. Alù, C. W. Qiu, T. J. Cui, *Nat. Commun.* **2019**, *10*, 1082.
- [12] L. Li, Y. Shuang, Q. Ma, H. Li, H. Zhao, M. Wei, C. Liu, C. Hao, C. W. Qiu, T. J. Cui, *Light: Sci. Appl.* **2019**, *8*, 97.
- [13] Y. B. Li, L. L. Li, B. B. Xu, W. Wu, R. Y. Wu, X. Wan, Q. Cheng, T. J. Cui, *Sci. Rep.* **2016**, *6*, 23731.
- [14] L. Zhang, X. Q. Chen, S. Liu, Q. Zhang, J. Zhao, J. Y. Dai, G. D. Bai, X. Wan, Q. Cheng, G. Castaldi, V. Galdi, T. J. Cui, *Nat. Commun.* **2018**, *9*, 4334.
- [15] J. Zhao, X. Yang, J. Y. Dai, Q. Cheng, X. Li, N. H. Qi, J. C. Ke, G. D. Bai, S. Liu, S. Jin, A. Alù, T. J. Cui, *Natl. Sci. Rev.* **2019**, *6*, 231.
- [16] T. J. Cui, S. Liu, G. D. Bai, Q. Ma, *Research* **2019**, *2019*, 2584509.
- [17] J. Y. Dai, W. K. Tang, J. Zhao, X. Li, Q. Cheng, J. C. Ke, M. Z. Chen, S. Jin, T. J. Cui, *Adv. Mater. Technol.* **2019**, *4*, 1900044.
- [18] J. Jiang, D. Sell, S. Hoyer, J. Hickey, J. Yang, J. A. Fan, *ACS Nano* **2019**, *13*, 8872.
- [19] J. Peurifoy, Y. Shen, L. Jing, Y. Yang, F. Cano-Renteria, B. G. DeLacy, J. D. Joannopoulos, M. Tegmark, M. Soljačić, *Sci. Adv.* **2018**, *4*, eaar4206.

- [20] J. S. Jensen, O. Sigmund, *Laser Photonics Rev.* **2011**, 5, 308.
- [21] M. B. Giles, N. A. Pierce, *Flow Turbul. Combust.* **2000**, 65, 393.
- [22] R. L. Johnston, *Dalton Trans.* **2003**, 0, 4193.
- [23] N. S. Froemming, G. Henkelman, *J. Chem. Phys.* **2009**, 131, 234103.
- [24] Y. LeCun, Y. Bengio, G. Hinton, *Nature* **2015**, 521, 436.
- [25] I. Goodfellow, Y. Bengio, A. Courville, *Deep Learning*, MIT Press, Cambridge **2016**.
- [26] X. Lin, Y. Rivenson, N. T. Yardimci, M. Velí, Y. Luo, M. Jarrahi, A. Ozcan, *Science* **2018**, 361, 1004.
- [27] Z. C. Wu, M. Zhou, E. Khoram, B. Y. Liu, Z. F. Yu, *Photonics Res.* **2020**, 8, 46.
- [28] Y. Shen, N. C. Harris, S. Skirlo, M. Prabhu, T. Baehr-Jones, M. Hochberg, X. Sun, S. Zhao, H. Larochelle, D. Englund, M. Soljačić, *Nat. Photonics* **2017**, 11, 441.
- [29] T. W. Hughes, I. A. Williamson, M. Minkov, S. Fan, *Sci. Adv.* **2019**, 5, eaay6946.
- [30] T. Qiu, X. Shi, J. Wang, Y. Li, S. Qu, Q. Cheng, T. J. Cui, S. Sui, *Adv. Sci.* **2019**, 6, 1900128.
- [31] A. Y. Piggott, J. Lu, K. G. Lagoudakis, J. Petykiewicz, T. M. Babinec, J. Vučković, *Nat. Photonics* **2015**, 9, 374.
- [32] M. H. Tahersima, K. Kojima, T. Koike-Akino, D. Jha, B. Wang, C. Lin, K. Parsons, *Sci. Rep.* **2019**, 9, 1368.
- [33] Q. Zhang, C. Liu, X. Wan, L. Zhang, S. Liu, Y. Yang, T. J. Cui, *Adv. Theory Simul.* **2019**, 2, 1800132.
- [34] D. Liu, Y. Tan, E. Khoram, Z. Yu, *ACS Photonics* **2018**, 5, 1365.
- [35] Z. Liu, D. Zhu, S. P. Rodrigues, K. T. Lee, W. Cai, *Nano Lett.* **2018**, 18, 6570.
- [36] S. So, J. Rho, *Nanophotonics* **2019**, 8, 1255.
- [37] A. Radford, L. Metz, S. Chintala, arXiv:1511.06434v2 [cs.LG] (accessed: January 2016).
- [38] M. Arjovsky, S. Chintala, L. Bottou, in *Proc. of Machine Learning Research* (Eds: D. Precup, Y. W. Teh), Vol. 70, PMLR, Sydney, Australia **2017**, p. 214.
- [39] M. Decker, I. Staude, M. Falkner, J. Dominguez, D. N. Neshev, I. Brener, T. Pertsch, Y. S. Kivshar, *Adv. Opt. Mater.* **2015**, 3, 813.
- [40] I. Goodfellow, J. Pouget-Abadie, M. Mirza, B. Xu, D. Warde-Farley, S. Ozair, A. Courville, Y. Bengio, in *Proc. of the 27th Int. Conf. on Neural Information Processing Systems*, Vol. 2, MIT Press, Cambridge, MA, USA **2014**, p. 2672.